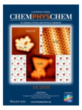

Formation of Two-Dimensional Copper Selenide on Cu(111) at Very Low Selenium Coverage

Holly Walen,[a, e] Da-Jiang Liu,[b] Junepyo Oh,[c] Hyun Jin Yang,[c, f] Yousoo Kim,[c] and Patricia A. Thiel*[a, b, d]

Using scanning tunneling microscopy (STM), we observed that adsorption of Se on Cu(111) produced islands with a $(\sqrt{3}\times\sqrt{3})R30^\circ$ structure at Se coverages far below the structure's ideal coverage of 1/3 monolayer. On the basis of density functional theory (DFT), these islands cannot form due to attractive interactions between chemisorbed Se atoms. DFT showed that incorporating Cu atoms into the $\sqrt{3}$-Se lattice stabilizes the structure, which provided a plausible explanation for the experimental observations. STM revealed three types of $\sqrt{3}$ textures. We assigned two of these as two-dimensional layers of strained CuSe, analogous to dense planes of bulk klockmannite (CuSe). Klockmannite has a bulk lattice constant that is 11% shorter than $\sqrt{3}$ times the surface lattice constant of Cu(111). This offers a rationale for the differences observed between these textures, for which strain limits the island size or distorts the $\sqrt{3}$ lattice. STM showed that existing step edges adsorb Se and facet toward $\langle 1\bar{2}1\rangle$, which is consistent with DFT.

1. Introduction

Metal chalcogenides provoke interest on the basis of properties as diverse as superconductivity and catalytic activity.[1,2] For example, a single layer of iron selenide is a surprisingly good superconductor, with a (relatively) high critical temperature of 65 K.[3,4] Tungsten and molybdenum dichalcogenides, such as MoS_2, are good hydrodesulfurization catalysts.[5] Recent interest in metal chalcogenides has also been spurred by their potential application in advanced energy conversion and storage devices. Copper selenides show unique properties for applications in photovoltaic and thermoelectric materials,[6–8] and copper chalcogenide based semiconductors are used in solar cells due to their high optical absorption efficiency.[9,10] Many metal chalcogenides are two-dimensional (layered) compounds, a fact that naturally raises interest in their preparation and use as two-dimensional sheets or films. In this paper, we show that two-dimensional copper selenide forms spontaneously on Cu(111) at room temperature, even at very low coverage of Se—less than 0.1 monolayer (ML). The reactants are simply $Se_{2(g)}$ and the Cu surface itself, in ultrahigh vacuum (UHV).

Previously, Nagashima et al.[11–13] studied the adsorption of Se on Cu(111) over a wide range of coverages at room temperature and above and in UHV. They deposited Se onto a Cu(111) film supported on mica, and the resultant surface was primarily analyzed with low energy electron diffraction (LEED), Auger electron spectroscopy, transmission electron microscopy, and electron energy loss spectroscopy. At 300 K, LEED showed a $(\sqrt{3}\times\sqrt{3})R30^\circ$ structure at low coverage, which was assigned as chemisorbed Se.[11] This was followed by formation of a CuSe overlayer and, eventually, a CuSe multilayer alloy.[12,13] The CuSe overlayer and alloy also exhibited $(\sqrt{3}\times\sqrt{3})R30^\circ$ LEED patterns, with evidence of a 6 to 7% (real-space) contraction relative to the initial structure.[12,13] Our experimental work is different from that of Nagashima et al. because it provides real-space images of the surface structures by scanning tunneling microscopy (STM), and it focuses on the very low coverage regime. In addition, we use density functional theory (DFT) to interpret the experimental data. Together, these features provide new insight. In particular, they lead to a re-interpretation of the $(\sqrt{3}\times\sqrt{3})R30^\circ$ structure at low coverage as being due to islands of CuSe, rather than chemisorbed Se.

This paper is divided into five sections. Section 2 provides the experimental observations and the relevant calculations. Section 3 discusses the results and draws some comparison to S/Cu(111) and two-dimensional dichalcogenides. Section 4 contains the conclusions of this work. Finally, the last section gives details of the experimental and computational work. The Supporting Information contains some additional experimental in-

---

[a] Dr. H. Walen, Prof. P. A. Thiel
Department of Chemistry, Iowa State University, Ames, IA 50011 (USA)
E-mail: pthiel@iastate.edu

[b] Dr. D.-J. Liu, Prof. P. A. Thiel
Ames Laboratory of the USDOE, Ames, IA 50011 (USA)

[c] Dr. J. Oh, Dr. H. J. Yang, Dr. Y. Kim
Surface and Interface Science Laboratory, RIKEN, Wako, Saitama 351-0198 (Japan)

[d] Prof. P. A. Thiel
Department of Materials Science & Engineering, Iowa State University, Ames, IA 50011 (USA)

[e] Dr. H. Walen
Current address: Surface and Interface Science Laboratory, RIKEN, Wako, Saitama 351-0198 (Japan)

[f] Dr. H. J. Yang
Current address: University College London, London, WC1E 6BT (UK)

Supporting Information for this article can be found under: http://dx.doi.org/10.1002/cphc.201600207.

formation, as well as computational results that are peripheral to the arguments and conclusions in this manuscript.

2. Results

2.1. Experimental Results

2.1.1. Features on Terraces

Figure 1 a shows an image of the clean Cu(111) surface with atomic resolution, which allows definition of the crystallographic directions as shown beside the panel. Upon adsorption of Se, we observe individual, dotlike protrusions, two of which are evident on the left of Figure 1 b. The individual protrusions have a width (measured at full-width at half-maximum, FWHM) of (0.52 ± 0.08) nm ($N = 76$), height of (0.05 ± 0.01) nm ($N = 76$), and area of (0.23 ± 0.05) nm^2 ($N = 58$).

In addition to these features, islands form on the surface, even though the coverage is very low (< 0.10 ML). The islands display three types of internal textures. In the first (type A), protrusions are arranged hexagonally. Each protrusion is defined by a circular outline. Examples are shown in Figure 1 b–e. The nearest-neighbor separation between protrusions is $\sqrt{3}a$ [measured spacing = (0.45 ± 0.02) nm, $\sqrt{3}a = 0.442$ nm], rotated by 30° from the close-packed directions, that is, parallel to $\langle 1\bar{2}1 \rangle$. Hence, the internal structure is $(\sqrt{3}\times\sqrt{3})R30^{\circ}$, which we abbreviate as $\sqrt{3}$. The island edges are often facetted parallel to $\langle 1\bar{2}1 \rangle$. In other cases, the protrusions at the island edge are arranged irregularly, as if protrusions have just joined or left the island. Islands with exclusively type A texture are made up of 20 or fewer protrusions, corresponding to an area ≤ 4 nm^2.

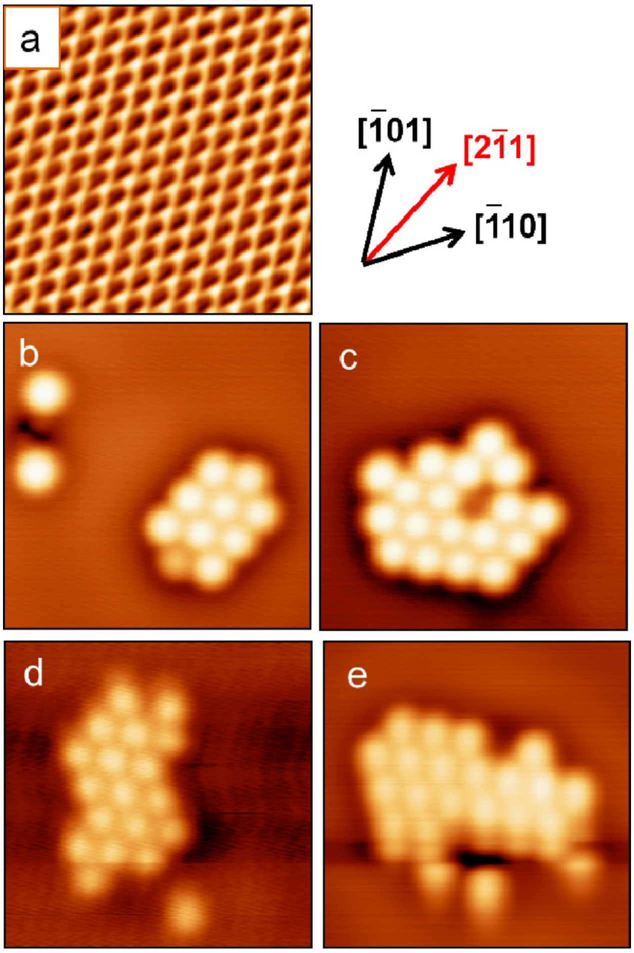

Figure 1. Topographic STM images. a) Atomically resolved Cu(111), 3×3 nm^2. Two close-packed directions and one open direction are labelled to the right of panel a. b–e) Examples of islands with type A texture, 4×4 nm^2.

In the second type of internal structure (type B), the surface is smoother, with a $\sqrt{3}$ arrangement of small depressions. Examples are shown in Figure 2 a–d. Type B regions have triangular footprints, with edges again aligned parallel to $\langle 1\bar{2}1 \rangle$. Areas are in the range of 1 to 3 nm^2, that is, comparable to those of type A regions. Type B and A regions can coexist in a single island; Figure 2 a–c shows examples of such hybrids. It is rare to find an island that is entirely type B, such as in Figure 2 d, whereas it is common to find one entirely type A, such as in Figure 1 a–d. This, plus the comparable range of sizes, suggests that type A transforms into type B and that the hybrid islands represent incomplete transformations.

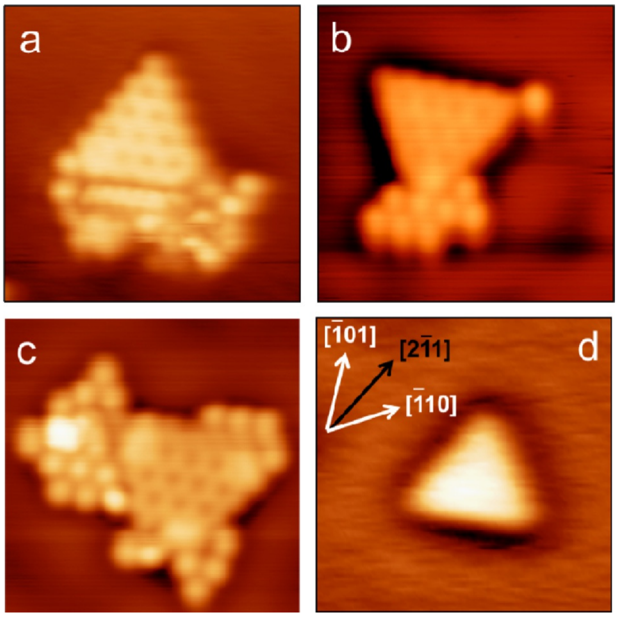

Figure 2. Topographic STM images of islands containing type B texture, all 5×5 nm^2. In panels a–c, some type A texture is also present in the island.

The third texture (type C) is characteristic of islands with a much larger area of > 100 nm^2 (Figure 3). Type C resembles type B in the sense that it has a $\sqrt{3}$-like pattern defined by individual small depressions in a smooth matrix. However, in type C a long-range, linear corrugation is superposed. The separation between corrugation lines alternates regularly between 1.8 and 2.0 nm. This alternation is most clear in Figure 3 c. The corrugation is shallow, (0.004 ± 0.001) nm ($N = 2$). Type C islands are usually connected along one side to a step edge, as in Figure 3 a, b, which is indicative of growth outward from steps. The average height is (0.06 ± 0.01) nm ($N = 4$), which is much smaller than that of a single Cu(111) step, 0.208 nm.[14]

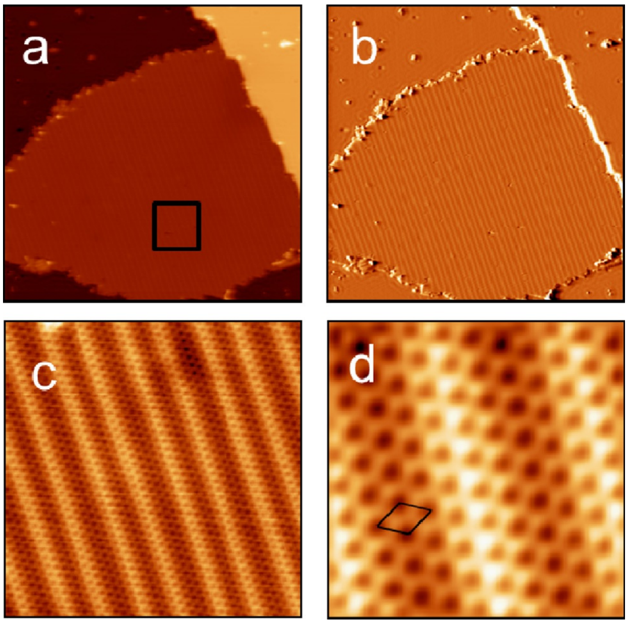

Figure 3. STM images of an island with type C texture. One island is shown as a) topographic and b) derivative images, 100×100 nm^2. c) Topographic image (15×15 nm^2) of the area defined by the square in panel a. d) Topographic image (4×4 nm^2) with the $\sqrt{3}$ unit cell drawn as a black rhombus.

The corrugation is shown for four additional type C islands in Figure 4. All exhibit contraction in the $\sqrt{3}$-like pattern of depressions, along the two directions close to $\langle 1\bar{2}1\rangle$ that cross the corrugation line. (These directions are illustrated by arrows at the top of Figure 4a.) The degree of contraction, relative to $\sqrt{3}a$, is unequal in the two directions and is 2 to 4% and 4 to 8%, respectively. (We estimate 2% deviation as the limit of detection in these experiments.) In some cases, the texture parallel to the corrugation is rotated by approximately 1°. The rotation is present in Figure 4c but not in Figure 4a. These features, and their subtle variation among different islands, suggest the existence of a set of coincidence lattices that are similar in structure and close in energy. Their development or stability may be influenced by the adjoining step edge.

2.1.2. Step Edge Decoration

Exposure to Se causes steps along Cu terraces to facet along $\langle 1\bar{2}1\rangle$ directions (Figure 5). The faceted steps are decorated by a regularly spaced line of protrusions that we assign as Se atoms. The spacing between these protrusions is (0.44±0.02) nm, in agreement with $\sqrt{3}a$ spacing (0.442 nm). It is also common to find small islands attached to step edges, such as the one shown in Figure 5b.

2.2. Computational Results

The goal of the computational work is to identify viable structural candidates for the features observed by STM. One metric is the level of agreement between the measured STM image and the simulated image of an energy-optimized configuration derived from DFT. The other metric is the chemical potential of Se, μ_{Se}, which we will use in two forms: $\mu_{Se}{}^{0}$ for the flat Cu(111) surface, relevant to Se on terraces, and $\mu_{Se}{}^{hkl}$ for surfaces vicinal to Cu(111), relevant to Se at steps. These two cases are addressed sequentially below.

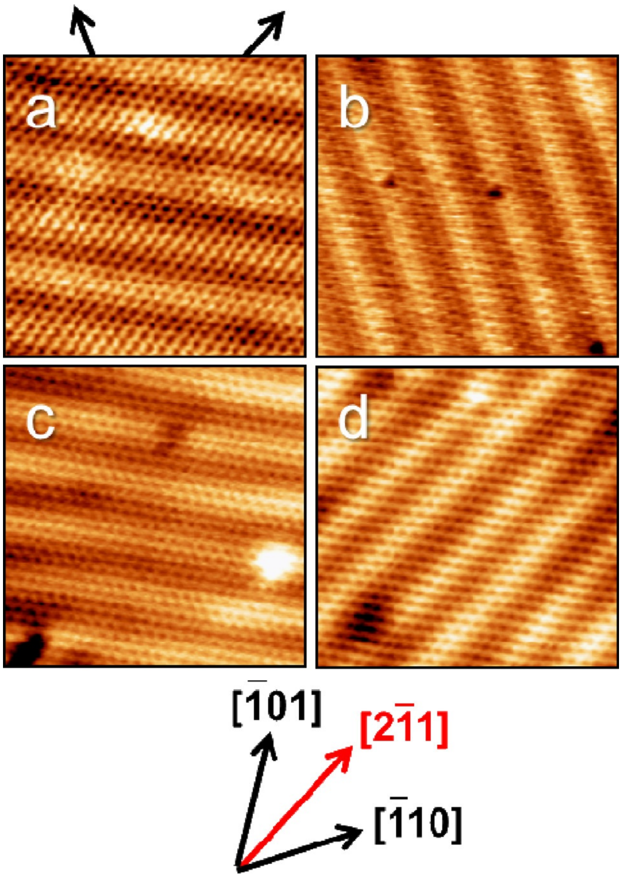

Figure 4. Topographic STM images of different type C islands, all 10×10 nm^2. The arrows at the top of panel a define the directions of the $\sqrt{3}$-like lattice that cross the corrugation in this particular island.

2.2.1. Features on Terraces

Physically, $\mu_{Se}{}^{0}$ reflects the change in energy per Se when Se adsorbs on terraces, possibly in the form of Cu–Se structures, given an unlimited supply of Cu available from steps/kinks (at 0 K). We define it as [Eq. (1)]:

$$\mu_{Se}{}^{0} = \frac{[E(\mathrm{Cu}_m\mathrm{Se}_n + \mathrm{slab}) - E(\mathrm{slab}) - m\mu_{Cu}]}{n} - \frac{E(\mathrm{Se}_{2,g})}{2} \tag{1}$$

in which E is energy and μ_{Cu} is the chemical potential of Cu in the bulk metal (at 0 K), which also corresponds to the bulk cohesive energy. If bulk and surface are equilibrated, μ_{Cu} is equivalent to the binding energy of a Cu atom at a step kink site.[15] The integers m and n are the numbers of Cu and Se atoms in the complex, respectively. If $m=0$, $\mu_{Se}{}^{0}$ reduces to the adsorption energy, E_b, of a Se adatom. With this definition, a negative value of E_b indicates exothermic adsorption and a more negative $\mu_{Se}{}^{0}$ represents a more stable structure. We use the energy of gaseous triplet Se_2 as $E(Se_{2,g})$.

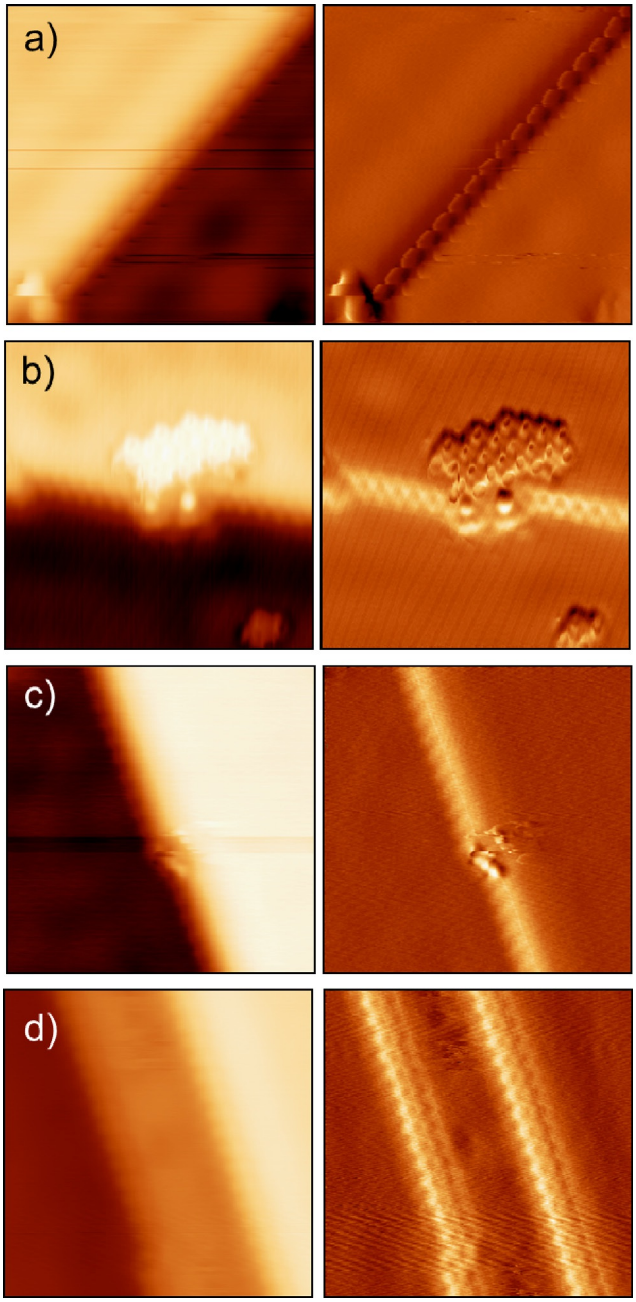

Figure 5. STM images of Se-decorated step edges. The left column contains topographic images, the right column contains derivative images. a) 5.8×6 nm^2 and b–d) 7×7 nm^2.

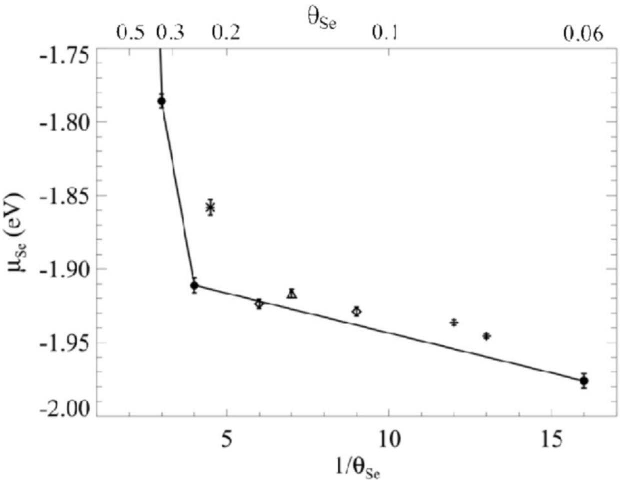

Figure 6. Chemical potential of Se as a function of inverse Se coverage (θ_{Se}) for a variety of supercells. The solid line is defined by the p(4×4) (1/16 ML), p(2×2) (1/4 ML), and ($\sqrt{3}\times\sqrt{3}$)R30° (1/3 ML) supercells.

Calculations in a (2×2) supercell show that the most favorable site for Se is the face-centered cubic (fcc) site, with the hexagonal close–packed site 0.042(1) eV less favorable. Figure 6 shows $\mu_{Se}{}^0$ as a function of (inverse) Se coverage for a variety of supercells with Se at fcc sites. If plotted in this way, the stability of the system is represented by the convex hull.[16] In Figure 6 this is shown by the solid line, for which it is defined by p(4×4), p(2×2), and $\sqrt{3}$ supercells. The lowest coverage examined theoretically, which is that of the p(4×4), equals the highest coverage in experiments, 0.06 ML. For this, $\mu_{Se}{}^0 = -1.975$ eV, and this value is lower than that of either of the other two structures on the convex hull. Thus, from DFT there is no mechanism to form $\sqrt{3}$ islands of Se atoms at the low coverage probed in experiment.

The predominance of the $\sqrt{3}$ structure in experiments leads us to take a different approach. Starting from the $\sqrt{3}$ structure of chemisorbed Se, we explore factors that may stabilize it. We begin by embedding Cu atoms in the Se matrix. Comparing $\mu_{Se}{}^0$ in Figure 7a–c shows that additional Cu can indeed stabilize the $\sqrt{3}$-Se structure. The most stable configuration has a Cu/Se ratio of 2:3, as shown in Figure 7c. In the simulated STM image, Se atoms produce round protrusions in a $\sqrt{3}$ pattern similar to that in type A texture. However, the image also exhibits very small dark regions in a p(3×3) pattern (reflecting the arrangement of added Cu atoms) and this is not observed experimentally. Nonetheless, because of the round protrusions and low chemical potential, we consider this a candidate structure for the type A texture.

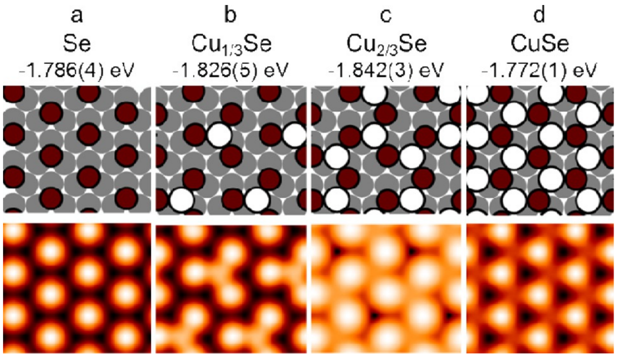

Figure 7. Configurations containing a fixed $\sqrt{3}$ lattice of Se atoms with various amounts of Cu. Lower panels show simulated STM images of each configuration. a) $\sqrt{3}$-Se, b) $\sqrt{3}$-$Cu_{1/3}Se$, c) $\sqrt{3}$-$Cu_{2/3}Se$, and d) $\sqrt{3}$-CuSe.

Adding more Cu atoms produces a 1:1 CuSe structure (Figure 7d) with a value of $\mu_{Se}{}^0$ that is not favorable relative to that of $Cu_{2/3}Se$. However, the compressed $\sqrt{3}$ lattice associated with type C texture indicates that strain plays a role. To approximate strain in an extended structure, we perform DFT calculations by using larger supercells derived from the $\sqrt{3}$-CuSe structure, with compression along only one of the principal $\sqrt{3}$ axes. There are many such unit cells that can be considered. We explored the set listed in Table 1, from which we conclude that those with coverage close to 0.36 ML (8% compression) are optimal. Figure 8 shows the lowest-energy configuration found in this search, with a value of $\mu_{Se}{}^0$ that is 0.039 eV lower than that of the uncompressed $\sqrt{3}$-CuSe structure in Figure 7d. (These comparisons can also be made by using Table 2, which summarizes key values of $\mu_{Se}{}^0$ presented in this section.) The simulated STM image in Figure 8 shows that the linear corrugation is reproduced qualitatively.

Table 1. Values of $\mu_{Se}{}^0$ for various large supercells derived from $(\sqrt{3}\times\sqrt{3})$R30°, with compression along one of the principal $\sqrt{3}$ axes. Uncertainty in the third decimal place of $\mu_{Se}{}^0$ is given in parentheses. The supercells can be described with matrix notation, where the matrix $M=\begin{pmatrix}2 & 1\\ m_{21} & m_{22}\end{pmatrix}$ and the basis vectors $\utilde{a}_1$ and $\utilde{a}_2$ are defined in Figure 8. The unit cell area is normalized to that of the (1×1). Each *k*-point grid is specified for the actual supercell. The row in italics corresponds to the configuration shown in Figure 8.

Unit cell area	(m_{21}, m_{22})	Chemical potential [eV]	*k*-Point grid	Se coverage [ML]
3	(1,2)	−1.772(1)	(14×14×1)	0.333
5	(1,3)	−1.528(2)	(14×9×1)	0.400
7	(1,4)	−1.545(1)	(14×7×1)	0.429
8	(0,4)	−1.664(3)	(14×6×1)	0.375
10	(0,5)	−1.707(2)	(14×5×1)	0.400
11	(1,6)	−1.724(2)	(14×4×1)	0.364
12	(0,6)	−1.584(2)	(14×4×1)	0.417
13	(1,7)	−1.770(1)	(14×4×1)	0.385
14	(0,7)	−1.757(2)	(14×3×1)	0.357
16	(0,8)	−1.794(1)	(14×3×1)	0.375
17	(1,8)	−1.772(1)	(14×3×1)	0.353
18	(0,9)	−1.707(1)	(14×3×1)	0.389
19	(1,10)	−1.805(1)	(14×3×1)	0.368
20	(0,10)	−1.780(2)	(14×2×1)	0.350
21	(1,10)	−1.715(1)	(14×2×1)	0.381
22	(0,11)	−1.808(2)	(14×2×1)	0.364
23	(1,12)	−1.785(2)	(14×2×1)	0.348
24	(0,12)	−1.754(6)	(14×2×1)	0.375
25	*(1,13)*	*−1.811(1)*	*(14×2×1)*	*0.360*
27	(1,14)	−1.747(1)	(14×2×1)	0.370
28	(0,14)	−1.806(1)	(14×2×1)	0.357

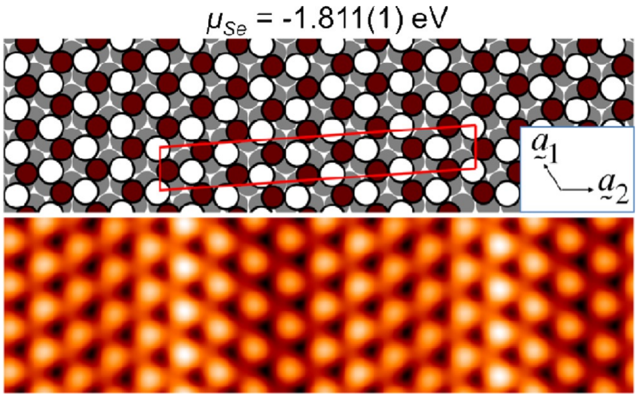

Figure 8. A $\begin{pmatrix}2 & 1\\ 1 & 13\end{pmatrix}$ approximant to $\sqrt{3}$-CuSe, with coverage 0.360 ML and area 25 times that of the (1×1). See Table 1. The red rhombus shows the primitive unit cell.

Table 2. Key values of μ^0_{Se} calculated from DFT. The *k*-point grids are specified for the actual supercells.

Structure	μ^0_{Se} [eV]	Supercell	*k*-Point grid	Figure	Island type
p(4×4)-Se	−1.975	(4×4)	(9×9×1)	n/a	
p(2×2)-Se	−1.911	(2×2)	(18×18×1)	n/a	
$\sqrt{3}$-Se	−1.786	$(\sqrt{3}$x$\sqrt{3})$R30°	(21×21×1)	7a	
$\sqrt{3}$-$Cu_{1/3}Se$	−1.828	(3×3)	(8×8×1)	7b	
$\sqrt{3}$-$Cu_{2/3}Se$	−1.842	(3×3)	(8×8×1)	7c	possible type A
$\sqrt{3}$-CuSe uncompressed	−1.772	$(\sqrt{3}\times\sqrt{3})$R30°	(14×14×1)	7d	
$\sqrt{3}$-CuSe compressed	−1.811	$\begin{pmatrix}2 & 1\\ 1 & 13\end{pmatrix}$	(14×2×1)	8	type C
$CuSe_3$ cluster	−1.904	(4×4)	(6×6×1)	9a	
Cu_3Se_6 cluster/island	−1.904	(5×5)	(5×5×1)	9b	possible type A
Cu_6Se_{10} island	−1.869	(6×6)	(4×4×1)	9c	
$Cu_{10}Se_{15}$ island	−1.875	(8×8)	(3×3×1)	9d	type B

The most favorable $\mu_{Se}{}^0$ found for the compressed structure must be an upper limit on $\mu_{Se}{}^0$ of the true structure. In the experimental data, there is evidence that contraction is not uniaxial and that the unit cell can rotate. The size and complexity make a more exhaustive DFT search computationally prohibitive. The calculations in hand demonstrate firmly, however, that the $\sqrt{3}$-CuSe layer is stabilized by contraction from the ideal $\sqrt{3}$ dimensions. We propose that type C texture arises from an extended, compressed $\sqrt{3}$-CuSe layer.

Another mechanism of strain relief is to limit the size of the islands, as strain scales with size. We therefore calculate $\mu_{Se}{}^0$ of various small, finite $\sqrt{3}$-CuSe islands in large supercells. These islands, shown in Figure 9, also have lower (more negative) $\mu_{Se}{}^0$ than the extended, uncompressed $\sqrt{3}$-CuSe structure of Figure 7d. (See also Table 2.) The most stable islands terminate with Se rather than Cu, as shown, and have a triangular shape with edges parallel to $\langle 1\bar{2}1\rangle$, as observed in experiment for type B regions. The simulated STM image of the largest island, $Cu_{10}Se_{15}$ in Figure 9d, has a texture resembling type B regions (Figure 1f–h)—small depressions on a smooth background. The triangular shape, edge orientation, internal texture, and reasonable stability all combine to support the assignment of type B regions as $\sqrt{3}$-CuSe islands, with size that is limited by strain.

The smaller Cu–Se islands in Figure 9b,c show protrusions reminiscent of type A texture. This, plus their reasonable value of $\mu_{Se}{}^0$, makes them candidates for type A structure.

Finally, we check for effects of the DFT functional on relative stability between chemisorbed Se and Cu–Se clusters. For this exercise, we compare the chemisorbed p(2×2) phase with Cu_3Se_6 in a (5×5) supercell. (The Cu_3Se_6 cluster is shown in Figure 9b, for which its value of $\mu_{Se}{}^0$ was calculated by using the

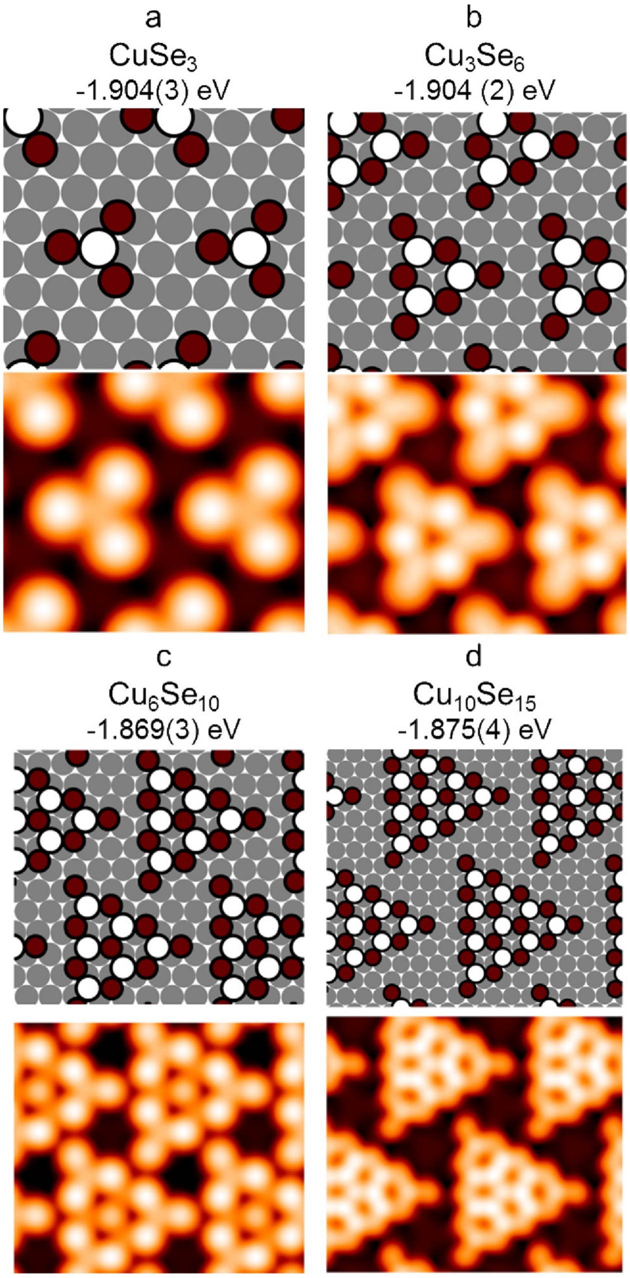

Figure 9. Configurations of small, triangular $\sqrt{3}$-CuSe islands with simulated STM images.

Perdew–Burke–Ernzerhof (PBE) functional—similar to that of all other structures illustrated in this paper and in the Supporting Information). With PBE, the p(2×2) is more stable by 0.006 eV. However, with local-density approximation (LDA), the p(2×2) is less stable by 0.025 eV, which is more consistent with experiment, as p(2×2) is never observed. Although we cannot conclude from this that LDA is better for Se/Cu(111) than PBE in general, it at least raises the possibility that approximations in the exchange-correlation functional could introduce errors large enough to shift the relative stabilities of chemisorbed Se and Cu–Se structures. Therefore, it is important to note that our assignments of structures in this system are based on both energetic trends and on matches with STM images.

2.2.2. Step Edges

On a clean Cu(111) surface, the close-packed step orientations are most stable. There are two kinds of such orientations, denoted here as α and β, that can be described as (100) and (111) microfacets, respectively. Experimentally, we observe that Se causes existing steps to facet along open $\langle 1\bar{2}1\rangle$ directions. To assess the energetics of this phenomenon, we must take into account the binding energy of Se at open versus dense steps, as well as the energy penalty associated with converting Cu steps from close-packed into open.

To do this, we perform calculations by using slabs with (stepped) surfaces that are vicinal to (111), specified by Miller indices (*hkl*). Slab surfaces are constructed to contain open steps or dense steps of either α or β type. Se atoms are placed at $\sqrt{3}a$ intervals on open steps to match the experimental data in Section 3.1 and at $2a$ intervals on the close-packed steps to match prior observations for S adsorbed at dense steps of Cu(111).[17] We evaluate $\mu_{\mathrm{Se}}{}^{0}$, as well as an additional chemical potential, $\mu_{\mathrm{Se}}{}^{hkl}$, defining the latter as [Eq. (2)]:

$$\mu_{\mathrm{Se}}{}^{hkl} = \mu_{\mathrm{Se}}{}^{0} + \{A(\gamma^{hkl} - \gamma^{111})\} \qquad (2)$$

in which A is the area of the supercell and γ is the surface energy per unit area. With reference to Equation (1), $n=1$ and $m=0$. By this definition and for the specified configurations of Se at steps, $\mu_{\mathrm{Se}}{}^{0}$ reflects the energy of Se adsorption at a step, whereas $\mu_{\mathrm{Se}}{}^{hkl}$ equals this plus the energy cost of creating a stepped (*hkl*) surface instead of a flat (111) surface.

The results are shown in Table 3. The quantity $\mu_{\mathrm{Se}}{}^{0}$ can be used to compare Se adsorption on the (111) terrace versus adsorption at a step. Recalling that $\mu_{\mathrm{Se}}{}^{0} = -1.975$ eV for Se chemisorbed on the terrace at low coverage (Table 2), one sees that values of $\mu_{\mathrm{Se}}{}^{0}$ for Se adsorbed at steps on the vicinal slabs are always lower. This shows that it is more favorable for Se to adsorb at an (existing) step than on a terrace, for either step orientation.

The quantity $\mu_{\mathrm{Se}}{}^{hkl}$ is useful for comparing the stability of open versus dense steps with adsorbed Se. We choose to compare supercells with Se coverages close to 0.1 ML, which repre-

Table 3. Chemical potentials of Se adsorbed at three kinds of steps on Cu surfaces that are vicinal to (111). The Se coverage is inversely proportional to the unit cell area and, for a fixed step type, to the width of the (111) microfacet. Samples are shown in Figure 10.

Step	h,k,l	$\mu_{\mathrm{Se}}{}^{0}$ [eV]	$\mu_{\mathrm{Se}}{}^{hkl}$ [eV]	Se coverage [ML]
open $\langle 1\bar{2}1\rangle$	11,9,7	−2.358	−1.884	0.126
open $\langle 1\bar{2}1\rangle$	6,5,4	−2.356	−1.891	0.114
open $\langle 1\bar{2}1\rangle$	13,11,9	−2.344	−1.875	0.104
average			−1.88	
close-packed α	3,2,2	−2.331	−1.860	0.121
close-packed α	4,3,3	−2.234	−1.842	0.086
average			−1.85	
close-packed β	5,5,3	−2.252	−1.839	0.130
close-packed β	3,3,2	−2.253	−1.791	0.107
average			−1.82	

sents the lower limit of coverage (upper limit of supercell size) that we can reliably assess. The three configurations that were evaluated are illustrated in Figure 10. Table 3 shows that $\mu_{\mathrm{Se}}{}^{hkl}$ is lowest for the open step, intermediate for the close-packed α step, and highest for the close-packed β step. Hence, it is energetically favorable for an existing Cu step to convert from close-packed into open upon adsorption of Se. This is consistent with experiment.

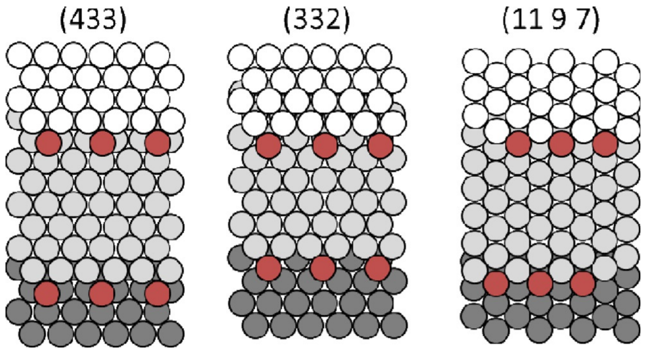

Figure 10. Three examples of Cu surfaces vicinal to (111). The energetics for these configurations are presented in Table 3.

3. Discussion

There are two main results from this work. First is the experimental observation of $\sqrt{3}$ islands exhibiting three distinctive textures at Se coverage far below the ideal $\sqrt{3}$ coverage of 1/3 ML. The second result comes from DFT, namely, the fact that attractive interactions between Se adatoms cannot account for the formation of these islands. DFT shows that incorporating Cu atoms into the $\sqrt{3}$-Se lattice stabilizes the structure, which provides a plausible explanation for the experimental observations. In particular, the DFT-based simulations of STM images provide good evidence for formation of two-dimensional CuSe islands.

To a large extent, our observations are compatible with the observations and interpretation of Nagashima et al.,[11–13] who studied Se/Cu(111) using techniques that yielded large-scale average information rather than microscopic images. They observed a $\sqrt{3}$ LEED pattern over a broad coverage range, which they attributed to chemisorbed Se (at low coverage), two-dimensional CuSe (at higher coverage), and eventually a three-dimensional CuSe alloy. The assignment of CuSe was based on relative Auger intensities for Cu and Se in the three-dimensional compound. We disagree only about the nature of $\sqrt{3}$ in its early stages, which we argue must include Cu atoms as well as Se.

STM reveals three types of $\sqrt{3}$ textures in the islands. We assign two of these as two-dimensional layers of CuSe. In type B texture, the $\sqrt{3}$ is epitaxial but it has a small area. In type C texture, the $\sqrt{3}$ is distorted (contracted) by 2–8%, but covers a larger area. In both types B and C, the characteristics of limited size and distortion, respectively, can be attributed to strain. Nagashima et al.[12,13] deduced from LEED that the $\sqrt{3}$ lattice constant of high-coverage CuSe was contracted by 6–7% relative to that of the initial $\sqrt{3}$ pattern, consistent with our STM data for type C texture.

It is interesting to note that bulk CuSe—known as klockmannite—contains planes of atoms that are interpenetrating hexagonal networks of Cu and Se.[18] The atomic arrangement in such a plane is essentially identical to that shown in Figures 8 and 9d as models for textures of types C and B, respectively. However, the Cu–Cu separation in this plane is 11% shorter than $\sqrt{3}a$ on Cu(111), which provides a natural rationale for the strain-limited size of the epitaxial type B islands and the contraction in the type C islands.

The origin of type A texture, with its well-defined circular protrusions, is less certain. Using DFT, we identified two possibilities. One is a substoichiometric CuSe layer. In this vein, DFT calculations yielded optimal results for $\mathrm{Cu_{2/3}Se}$, but we speculate that the real structure may tolerate some disorder, as for our ideal $\mathrm{Cu_{2/3}Se}$ there is an additional periodicity that is not observed with STM. Disorder is also supported by the fact that a Cu-poor form of bulk klockmannite has been reported, $\mathrm{Cu_{0.87}Se}$, that exhibits disorder in the planar Cu–Se sheets.[19] The second possibility is that type A texture signals small or irregular regions of stoichiometric CuSe, as DFT shows that if a CuSe region is small enough it exhibits the circular-protrusion texture in STM, as shown in Figure 9b,c. This is less likely, however, as the border between type A and B textures is very clear in hybrid islands such as those in Figure 2a–c, and this implies a clear difference in structure. At present we must leave this issue unresolved.

We can compare the present results for Se/Cu(111) with prior results for S/Cu(111), obtained under similar experimental conditions of low coverage (up to 0.05 ML) and measurement at 5 K following adsorption at 300 K. Cu–S complexes are observed on terraces, and the smallest is heart-shaped $\mathrm{Cu_2S_3}$.[20] Larger complexes also exist, and they become more abundant with increasing coverage. These are chains consisting of concatenated $\mathrm{Cu_2S_3}$. At 0.05 ML, Cu–S complexes are replaced by a low-density $(\sqrt{43}\times\sqrt{43})\mathrm{R}\pm 7.5^\circ$ reconstruction.[17,21,22] The $\mathrm{Cu_2S_3}$ and chain structures are stabilized by a linear S–Cu–S motif.[17,20] We do not observe analogous structures in the Cu–Se system, although the $\sqrt{3}$ islands incorporate both Cu and Se, as in the Cu–S complexes. It is likely that multiple factors contribute to this difference. One is simply the lattice mismatch between Cu(111) and the chalcogenide CuX (X = S, Se), which is 14% for the sulfide[23] but only 11% for the selenide.[18] Another factor may be electronic structure. In bulk metal chalcogenides, it is known that upon progressing from sulfides to selenides to tellurides, bonding becomes less ionic and electrons become more delocalized.[5] If delocalization is more important for stabilizing Cu–Se than Cu–S moieties, this could account for the formation of extended, dense $\sqrt{3}$ structures with Se, but smaller complexes with S.

Finally, two-dimensional dichalcogenides, such as $\mathrm{MoX_2}$ and $\mathrm{WX_2}$, share some similarities with our Cu–Se type B islands. Islands of Mo and W dichalcogenides grow with perfect triangular shape on Au(111) and on some oxide surfaces[24–27] and are terminated at the edges with S or Se.[28,29] Both of these features are exhibited by the type B islands (Figure 9d), which have perfect triangular shape and are terminated by Se. However, our type B islands are a single layer of Cu–Se, whereas the dichalcogenide structures contain three atomic layers, wherein a metal layer is sandwiched between two chalcogenide layers.[25,28]

4. Conclusions

We observed that Se adsorption on Cu(111) produced islands with three types of $\sqrt{3}$ texture, far below the ideal Se coverage of 1/3 monolayer. The first of these, type A, consists of clearly defined round protrusions. Type A may reflect small regions of CuSe or Cu-deficient CuSe. The other two textures, types B and C, are both assigned as two-dimensional layers of CuSe, for which strain limits the island size (type B) or distorts the $\sqrt{3}$ lattice (type C). These two types of structures are analogous to dense planes of bulk klockmannite, CuSe. The observed compression in the type C islands is accounted for in terms of the bulk CuSe lattice constant, which is 11% shorter than $\sqrt{3}a$ on Cu(111). In both types, Se forms dense $\sqrt{3}$ islands that incorporate Cu. This is in contrast to S, which forms small complexes with Cu under comparable conditions on Cu(111).[17,20]

Experimental and Computational Details

Experimental Conditions

Experiments were performed at the Surface and Interface Science Laboratory at RIKEN in Japan. Experiments were conducted in an ultrahigh vacuum chamber equipped with low-temperature (5 K) STM and an electrochemical source for in situ $Se_{2(g)}$ deposition.[30,31]

Cu(111) was cleaned by sputtering with Ar^+ (12–15 μA, 2.0 kV) for 10 min with the sample held at 850 K. This was done several times, keeping the sample at 850 K for 5 min between sputtering. The surface temperature was measured by optical pyrometry, and the precision was within 10 K. For the last cycle, the sample was allowed to cool while the surface was sputtered for an additional 3 min.

The piezo calibration parallel to the surface was checked by using atomically resolved images of terraces such as that in Figure 1a. The measured nearest-neighbor (NN) separation was (0.26 ± 0.01) nm, in agreement with the bulk value of 0.255 nm. The vertical calibration was checked by using atomic steps, for which the measured height of (0.20 ± 0.01) nm also agreed with the bulk value of 0.208 nm.[14]

During exposure to $Se_{2(g)}$, the sample was held at room temperature to promote dissociative adsorption. All STM images were acquired at 5 K. The sample was moved into the STM stage about 5 min after deposition, in which cooling lasted another 50 min. After an initial set of images was obtained, the sample was brought out of the STM stage and allowed to warm up to room temperature, followed by a subsequent quench to 5 K for the remainder of the experiment. This thermal cycling had no effect on the observed structures.

Typical tunneling conditions were within the following ranges: -1 to $+1$ V sample bias and 1.00 to 2.06 nA tunneling current. Exact tunneling conditions for each image are given in the Supporting Information. Tunneling in this range of parameters did not disturb the adsorbed species or change their dimensions. All STM images were planed using WSxM software.[32]

The coverage of Se was determined by counting distinct protrusions, whether isolated or in type A structures (as defined in the Results Section) and assigning 1 Se atom per protrusion. For type B and C structures, the area was evaluated and ideal coverages of 0.33 and 0.36 were assigned, respectively. Only terraces were included in this calculation. Step edges were disregarded. The data were collected over two experiments, in which Se coverage was 0.02 and 0.06 ML. There was no significant difference in the features observed at these two coverages.

Computational Description

DFT calculations were performed with the VASP code by using the PBE exchange-correlation functional with 280 eV energy cut off. Unless noted otherwise, results were obtained by averaging over slab thicknesses from 4 to 7 Cu layers and by using *k*-point grids corresponding to $(24\times24\times1)$ or $(36\times36\times1)$ for the primitive (1×1) unit cell or as close to those settings as possible.

In most calculations, slabs had (111) surface orientation but some had vicinal orientation. For these, *k*-point grids of $(36\times36\times1)$ in the (1×1) cell were needed to ensure convergence and to obtain reliable energetics. The vicinal slabs were comparable in thickness to the (111) slabs, though more layers were needed to achieve this, as atomic planes were less dense and more closely spaced in the vicinal slabs.

DFT was used to generate STM images for optimized configurations by mapping the isosurface of partial charge density, after Tersoff and Hamann.[33,34] The charge density was integrated over an energy window within ±0.1 eV of the Fermi energy.

Acknowledgements

The experimental component of this work was conducted or supervised by H.W., J.O., H.J.Y., Y.K., and P.A.T. with support from three sources. In the U.S., it was supported by the National Science Foundation (NSF) Grant CHE-1507223. In Japan, it was supported by a Grant-in-Aid for Scientific Research on Priority Areas "Electron Transport Through a Linked Molecule in Nano-scale" and by a Grant-in-Aid for Scientific Research(S) "Single Molecule Spectroscopy using Probe Microscope" from the Ministry of Education, Culture, Sports, Science, and Technology (MEXT). The theoretical component of this work was conducted by D.J.L., with support from the Division of Chemical Sciences, Basic Energy Sciences, U.S. Department of Energy (DOE). The theoretical component of the research was performed at Ames Laboratory, which is operated for the U.S. DOE by Iowa State University under contract No. DE-AC02-07CH11358. This part also utilized resources of the National Energy Research Scientific Computing Center, which is supported by the Office of Science of the U.S. DOE under Contract No. DE-AC02-05CH11231. We thank Gordon J. Miller for providing insight into the structure of bulk klockmannite.

Keywords: chalcogenides · selenides · copper · density functional theory · scanning tunneling microscopy

[1] M. Chhowalla, H. S. Shin, G. Eda, L.-J. Li, K. P. Loh, H. Zhang, *Nat. Chem.* **2013**, *5*, 263–275.
[2] M.-R. Gao, Y.-F. Xu, J. Jiang, S.-H. Yu, *Chem. Soc. Rev.* **2013**, *42*, 2986–3017.
[3] Q.-Y. Wang, Z. Li, W.-H. Zhang, Z.-C. Zhang, J.-S. Zhang, W. Li, H. Ding, Y.-B. Ou, P. Deng, K. Chang, J. Wen, C.-L. Song, K. He, J.-F. Jia, S.-H. Ji, Y.-Y. Wang, L.-L. Wang, X. Chen, X.-C. Ma, Q.-K. Xue, *Chin. Phys. Lett.* **2012**, *29*, 037402.
[4] D. Liu, W. Zhang, D. Mou, J. He, Y.-B. Ou, Q.-Y. Wang, Z. Li, L. Wang, L. Zhao, S. He, Y. Peng, X. Liu, C. Chen, L. Yu, G. Liu, X. Dong, J. Zhang, C. Chen, Z. Xu, J. Hu, X. Chen, X. Ma, Q. Xue, X. J. Zhou, *Nat. Commun.* **2012**, *3*, 931.
[5] *Transition Metal Sulphides: Chemistry and Catalysis* (Eds.: T. Weber, R. Prins, R. A. van Santen), Kluwer, Dordrecht, **1998**, pp. 1–20.
[6] W. S. Chen, J. M. Stewart, R. A. Mickelsen, *Appl. Phys. Lett.* **1985**, *46*, 1095–1097.
[7] V. M. Sklyarchuk, Y. O. Plevachuk, *Semiconductors* **2002**, *36*, 1123–1127.
[8] H. Liu, X. Shi, F. Xu, L. Zhang, W. Zhang, L. Chen, Q. Li, C. Uher, T. Day, G. J. Snyder, *Nat. Mater.* **2012**, *11*, 422–425.
[9] P. Jackson, D. Hariskos, E. Lotter, S. Paetel, R. Wuerz, R. Menner, W. Wischmann, M. Powalla, *Prog. Photovoltaics* **2011**, *19*, 894–897.
[10] A. Walsh, S. Chen, S.-H. Wei, X.-G. Gong, *Adv. Energy Mater.* **2012**, *2*, 400–409.
[11] S. Nagashima, I. Ogura, *Appl. Surf. Sci.* **1988**, *33–34*, 450–456.
[12] S. Nagashima, I. Ogura, *Thin Solid Films* **1993**, *228*, 64–67.
[13] S. Nagashima, E. Fukuchi, I. Ogura, *Appl. Surf. Sci.* **1991**, *48–49*, 44–49.
[14] M. E. Straumanis, L. S. Yu, *Acta Crystallogr. Sect. A* **1969**, *25*, 676–682.
[15] J. Liu, C.-W. Wu, T. T. Tsong, *Phys. Rev. B* **1991**, *43*, 11595–11604.
[16] P. N. Abufager, G. Zampieri, K. Reuter, M. L. Martiarena, H. F. Busnengo, *J. Phys. Chem. C* **2014**, *118*, 290–297.
[17] H. Walen, D.-J. Liu, J. Oh, H. Lim, J. W. Evans, Y. Kim, P. A. Thiel, *J. Chem. Phys.* **2015**, *142*, 194711.
[18] V. Milman, *Acta. Crystallogr. Sect. B* **2002**, *58*, 437–447.
[19] H. Effenberger, F. Pertlik, *Neues Jahrb. Mineral. Monatsh.* **1981**, *1981*, 197–205.
[20] H. Walen, D.-J. Liu, J. Oh, H. Lim, J. W. Evans, C. Aikens, Y. Kim, P. A. Thiel, *Phys. Rev. B* **2015**, *91*, 045426.
[21] E. Wahlström, I. Ekvall, H. Olin, S. A. Lindgren, L. Walldén, *Phys. Rev. B* **1999**, *60*, 10699.
[22] E. Wahlström, I. Ekvall, T. Kihlgren, H. Olin, S. A. Lindgren, L. Walldén, *Phys. Rev. B* **2001**, *64*, 155406.
[23] H. T. Evans, Jr., J. A. Konnert, *Am. Mineral.* **1976**, *61*, 996–1000.
[24] T. F. Jaramillo, K. P. Jørgensen, J. Bonde, J. H. Nielsen, S. Horch, I. Chorkendorff, *Science* **2007**, *317*, 100–102.
[25] H. G. Füchtbauer, A. K. Tuxen, P. G. Moses, H. Topsøe, F. Besenbacher, J. V. Lauritsen, *Phys. Chem. Chem. Phys.* **2013**, *15*, 15971–15980.
[26] J.-K. Huang, J. Pu, C.-L. Hsu, M.-H. Chiu, Z.-Y. Juang, Y.-H. Chang, W.-H. Chang, Y. Iwasa, T. Takenobu, L.-J. Li, *ACS Nano* **2014**, *8*, 923–930.
[27] X. Wang, Y. Gong, G. Shi, W. L. Chow, K. Keyshar, G. Ye, R. Vajtai, J. Lou, Z. Liu, E. Ringe, B. K. Tay, P. M. Ajayan, *ACS Nano* **2014**, *8*, 5125–5131.
[28] S. Helveg, J. V. Lauritsen, E. Laegsgaard, I. Stensgaard, J. K. Nørskov, B. S. Clausen, H. Topsøe, F. Besenbacher, *Phys. Rev. Lett.* **2000**, *84*, 951.
[29] J. V. Lauritsen, J. Kibsgaard, S. Helveg, H. Topsøe, B. S. Clausen, E. Laegsgaard, F. Besenbacher, *Nat. Nanotechnol.* **2007**, *2*, 53–58.
[30] H. Reinhold, *Z. Elektrochem.* **1934**, *40*, 361–364.
[31] H. Keller, H. Rickert, D. Detry, J. Droward, P. Goldfinger, *Z. Phys. Chem. (Muenchen Ger.)* **1971**, *75*, 273–286.
[32] I. Horcas, R. Fernández, J. M. Gómez-Rodríguez, J. Colchero, J. Gómez-Herrero, A. M. Baro, *Rev.Sci. Instrum.* **2007**, *78*, 013705.
[33] J. Tersoff, D. R. Hamann, *Phys. Rev. Lett.* **1983**, *50*, 1998–2001.
[34] J. Tersoff, D. R. Hamann, *Phys. Rev. B* **1985**, *31*, 805–813.

Manuscript received: February 29, 2016
Accepted Article published: April 28, 2016
Final Article published: May 9, 2016